5. P. Beatus and U. Lendahl, *J. Neurosci. Res.* **54**, 125 (1998); I. Ahmad, P. Zagouras, S. Artavanis-Tsakonas, *Mech. Dev.* **53**, 73 (1995).
6. Fixed frozen sections and cells were preincubated in blocking solution [BS; 5% donkey serum, 1% bovine serum albumin, 0.1% glycine, 0.1% L-lysine, 0.4% Triton X-100 in phosphate-buffered saline (PBS)] for 1 hour at room temperature, and left overnight at 4°C in primary antibodies/BS: bTAN20, bhN6D [1:5 (*29, 34*)]; PGHN [1:1200 (*34*)]; IC [1:800; F. Logeat *et al*., *Proc. Natl. Acad. Sci. U.S.A.* **95**, 8108 (1998)]; 88-C (1:2000), J59 [1:1000 (*23*)]; TS1 [1:5 (*35*)]; NotchC-20, JaggedC-20 (1:250, Santa Cruz); TuJ1 (1:500, BAbCO); anti-synaptophysin (1:200, Sigma); and anti-BrdU (1:75, Becton-Dickinson)]. After washing in PBS, samples were incubated with Cy2, Cy3, and Cy5 conjugated secondary antibodies (1:300, Jackson Immunoresearch) for 45 min. Single optical images were collected on a MRC 1024 confocal microscope (Bio-Rad).
7. Supplement Web material is available at www.sciencemag.org/feature/data/1042942.shl.
8. M. Lecourtois and F. Schweisguth, *Curr. Biol.* **8**, 771 (1998); G. Struhl and A. Adachi, *Cell* **93**, 649 (1998).
9. E. H. Schroeter, J. A. Kisslinger, R. Kopan, *Nature* **393**, 382 (1998).
10. N. Šestan, thesis, Yale University (1999).
11. J. C. Aster *et al*., *J. Biol. Chem.* **272**, 11336 (1997).
12. Dorsal telencephalon was dissociated with 0.01% papain (Worthington), 0.1% neutral protease (Roche), and 0.01% DNase I (Sigma) in Hanks' balanced salt solution twice for 15 min at 37°C, and gently triturated. Single cells were resuspended in Neurobasal medium containing 2% B27, 5% fetal bovine serum (FBS), 2 mM L-glutamine, 1 mM sodium pyruvate, penicillin (100 U/ml), and streptomycin (100 μg/ml) (all from Gibco), plated on precoated glass cover slips (*24*) at LD and HD, and incubated at 37°C in 5% CO_2.
13. C. Akazawa, Y. Sasai, S. Nakanishi, R. Kageyama, *J. Biol. Chem.* **267**, 2187 (1992); Y. Sasai, R. Kageyama, Y. Tagawa, R. Shigemoto, S. Nakanishi, *Genes Dev.* **6**, 2620 (1992).
14. The Helios Gene Gun (Bio-Rad) was used to transfect neurons with CMV-based plasmids [phN1 FL, pNotch1 FL, pNotch1 ICD (amino acids 1758 to 2556), pNotch2 FL, pNotch2 ICD (amino acids 1701 to 2471) (*24, 34*); pnumb, pnumb-like (*26*); pdeltex, p4xwtCBF1-luc (*29*); pEGFP-N2 (Clontech); placZ]. DNA was precipitated onto ~35 mg of 1-μm gold microcarrier. Coprecipitation ratios: 25 μg of pEGFP-N2 1:3 with placZ or 1:1.5:1.5 with other plasmids; and 33 μg of p4xwtCBF1-luc 1:3 with placZ or 1:1:1 with other plasmids, to a total of 100 μg. The DNA was delivered into neurons at ~100 psi. Neurons were analyzed 48 hours after transfection. Enhanced green fluorescent protein (EGFP) autofluorescence was evenly distributed along the entire neurite. EGFP/lacZ coprecipitation resulted in ~95% efficiency of coexpression as early as 12 to 15 hours after transfection.
15. The cells were washed with PBS and lysed in 50 μl of lysis buffer. Cell extract (10 μl) was used to measure either luciferase activity or β-galactosidase activity.
16. J. J.-D. Hsieh *et al*., *Mol. Cell. Biol.* **16**, 952 (1996); F. M. Lu and S. E. Lux, *Proc. Natl. Acad. Sci. U.S.A.* **93**, 5663 (1996); J. J.-D. Hsieh, D. E. Nofziger, G. Weinmaster, S. D. Hayward, *J. Virol.* **71**, 1938 (1997).
17. D. Nofziger, A. Miyamoto, K. M. Lyons, G. Weinmaster, *Development* **126**, 1689 (1999).
18. For RT-PCR (Titan System, Roche), 100 ng of total RNA were isolated using TRIZOL (Gibco). Typical PCR cycle parameters were as follows: *HES* analysis, 5 min at 95°C, 45 s at 58°C, and 1.5 min at 72°C for 40 cycles; *Delta*/*Jagged* analysis, 30 s at 95°C, 30 s at 58°C, and 1 min at 72°C for 45 cycles. The PCR products were separated on a 1% gel, stained with ethidium bromide, purified, and sequenced. For primers, see (*7*).
19. T. L. Fletcher, P. De Camilli, G. Banker, *J. Neurosci.* **14**, 6695 (1994); A. N. van den Pol, K. Obrietan, A. B. Belousov, Y. Yang, H. C. Heller, *J. Comp. Neurol.* **399**, 541 (1998).
20. Randomly selected neurons ($n > 6000$) were imaged and coded to conceal their identity during the measuring (*24*). Neurites longer than 10 μm were traced and counted as branches. Statistical significance was determined by *t* test. Branching of neurites is presented as branching index (number of branches divided by mean neurite length per neuron) analyzed at 9 DIV, which elucidates the different incidence of branching between control lacZ-transfected neurons and other transfected neurons (lacZ = 100%). LD cultures: Notch1 ICD = 144.5 ± 9.3% ($P = 0.003$), Notch2 ICD = 157.8 ± 12.5% ($P = 0.003$). HD cultures: Nmb = 43.0 ± 1.3% ($P = 0.004$), Nbl = 31.3 ± 5.6% ($P < 0.0003$), Dx = 24.0 ± 5.1% ($P < 0.000006$).
21. S. Jarriault *et al*., *Mol. Cell. Biol.* **18**, 7423 (1998); L. Li *et al*., *Immunity* **8**, 43 (1998).
22. B. Varnum-Finney *et al*., *Blood* **91**, 4084 (1998).
23. S. Wang *et al*., *Neuron* **21**, 63 (1998).
24. H. Qi *et al*., *Science* **283**, 91 (1999).
25. To generate stably transfected cell lines, we transfected NIH 3T3 cells with 20 μg of plasmids [pDelta1, pJagged1 (*35*); phJ1^{EC}myc, amino acids 1 to 1046 (*22*)] and selected with G-418 (0.8 mg/ml) in 10-cm plates. At least two separate cell pools were generated for each plasmid and assayed for the expression of transfected genes. For coculture assays, 3T3 cells were grown in DMEM/F-12 with N2 (Gibco) and 5% FBS (*24*) until confluence. Neurons growing on the cover slips (5 and 12 mm) were placed on top of the monolayer, facing the 3T3 cells, and maintained for 20 to 24 hours.
26. J. M. Verdi *et al*., *Curr. Biol.* **6**, 1134 (1996).
27. W. Zhong, J. N. Feder, M.-M. Jiang, L.Y. Jan, Y. N. Jan, *Neuron* **17**, 43 (1996); W. Zhong, M.-M. Jiang, G. Weinmaster, L. Y. Jan, Y. N. Jan, *Development* **124**, 1887 (1997); Y. Wakamatsu, T. M. Maynard, S. U. Jones, J. A. Weston, *Neuron* **23**, 71 (1999).
28. K. Matsuno *et al*., *Nature Genet.* **19**, 74 (1998).
29. P. Ordentlich *et al*., *Mol. Cell. Biol.* **18**, 2230 (1998).
30. G. A. Dunn, *J. Comp. Neurol.* **143**, 491 (1971); P. Rakic, *ibid.* **146**, 335 (1972); V. H. Perry and R. Linden, *Nature* **297**, 683 (1982).
31. E. Giniger, *Neuron* **20**, 667 (1998); E. C. Olson *et al*., *Mol. Cell. Neurosci.* **12**, 281 (1998); R. Yavari, C. Adida, P. Bray-Ward, M. Brines, T. Xu, *Hum. Mol. Genet.* **7**, 1161 (1998); O. Berezovska *et al*., *Neuroscience* **93**, 433 (1999); P. Castella, J. A. Wagner, M. Caudy, *J. Neurosci. Res.* **56**, 229 (1999).
32. D. Price and S. S. Sisodia, *Annu. Rev. Neurosci.* **21**, 479 (1998).
33. O. Berezovska *et al*., *Mol. Brain Res.* **69**, 273 (1999); B. De Strooper *et al*., *Nature* **398**, 518 (1999); W. Song *et al*., *Proc. Natl. Acad. Sci. U.S.A.* **96**, 6959 (1999); G. Struhl and I. Greenwald, *Nature* **398**, 522 (1999); Y. Ye, N. Lukinova, M. Fortini, *ibid.*, p. 525.
34. P. Zagouras, S. Stifani, C. M. Blaumueller, M. L. Carcangiu, S. Artavanis-Tsakonas, *Proc. Natl. Acad. Sci. U.S.A.* **92**, 6414 (1995).
35. G. E. Gray *et al*., *Am. J. Pathol.* **154**, 785 (1999).
36. Bromodeoxyuridine (BrdU) was administered by intraperitoneal injections (50 mg/kg body weight). The morning of vaginal plug was designated E0.

37. We thank R. Mann for making human Delta and Jagged plasmids; G. Weinmaster and C. Hicks for 88C and J59 antibodies; A. Israel for IC antibodies; E. Mitsiadis for mouse Notch and Jagged plasmids; J. McGlade for Numb and Numb-like plasmids; T. Kadesch for CBF1-luc and Deltex plasmids; E. Nestler and J. Chen for use of the luminometer; and M. Ding, M. Donoghue, T. Haydar, and P. Mellman for technical assistance. Supported by NIH grants NS14841 (P.R.) and NS26084 (S.A.-T.).

23 June 1999; accepted 26 August 1999

All-Inorganic Field Effect Transistors Fabricated by Printing

Brent A. Ridley, Babak Nivi, Joseph M. Jacobson*

A solution of cadmium selenide nanocrystals was used to print inorganic thin-film transistors with field effect mobilities up to 1 square centimeter per volt second. This mobility is an order of magnitude larger than those reported for printed organic transistors. A field effect was achieved by developing a synthesis that yielded discretely sized nanocrystals less than 2 nanometers in size, which were free of intimately bound organic capping groups. The resulting nanocrystal solution exhibited low-temperature grain growth, which formed single crystal areas encompassing hundreds of nanocrystals. This process suggests a route to inexpensive, all-printed, high-quality inorganic logic on plastic substrates.

According to Moore's Law, the number of transistors per microelectronic chip has doubled every 18 months. However, the cost of a chip per unit of area has remained relatively static for more than two decades. Hence, there is interest in developing printing techniques for microelectronics fabrication that are inexpensive, allow fabrication on plastic substrates, and can cover large areas. The primary focus to date has been on organic materials for solution-based printing (*1–3*). Solution processable organic semiconductors such as poly(3-hexylthiophene) have demonstrated field effect mobilities of ~0.1 $cm^2\ V^{-1}\ s^{-1}$ (*3*). Theoretical considerations (*4*) and experiments with vacuum-deposited organic semiconductors such as pentacene (*5*) indicate that the mobilities in organic semiconductors may be fundamentally limited to values on par with that of amorphous silicon: ~1 to 2 $cm^2\ V^{-1}\ s^{-1}$. Although solution-processed organic thin-film transistors (TFTs) have been incorporated in

The Media Laboratory, Massachusetts Institute of Technology, 20 Ames Street, Cambridge, MA 02139, USA.

*To whom correspondence should be addressed. E-mail: jacobson@media.mit.edu

optoelectronic devices (*3*, *6*) and radio-frequency identification (RFID) tags (*2*), the low mobilities of these TFTs make them inappropriate for applications in microprocessors, display drivers, and active matrix backplanes for high-resolution displays (*7*).

Inorganic semiconductors are the basis for almost all high-performance microelectronic devices. They can have intrinsic mobilities of ~1000 $cm^2\ V^{-1}\ s^{-1}$, with lifetimes over 50 years and clock speeds beyond 1 GHz. Inorganic microelectronic devices are generally fabricated with techniques such as diffusion, thermal oxidation, ion implantation, photolithography, etching, evaporation, sputtering, chemical vapor deposition, and high-temperature (>1000°C) film growth. Unfortunately, inorganic semiconductors are not intrinsically soluble in any convenient solvents and do not offer structural variability as a mechanism to alter their solubility.

We describe a method for printing inorganic thin films by using stable nanocrystal solutions as precursors to polycrystalline thin films. Unlike a bulk crystal, the population of surface atoms in a nanocrystal is nonnegligible. Nanocrystals have properties somewhere between those of a bulk solid and an atomic species, and the physical, optical, and electrical properties of a nanocrystal are all functions of its size (*8*). The size-dependent melting point depression observed in nanocrystals (*9*–*12*) is critical to the work reported here. Nanocrystals have been reported to melt at temperatures 1000°C lower than their bulk melting temperature (*10*–*12*). Extreme melting point depressions enable the melting or sintering of nanocrystals into polycrystalline films at low temperatures. The use of nanocrystals as precursors to bulk thin films has been proposed by a number of researchers (*11*–*15*), but here we demonstrate that inorganic TFTs can be fabricated with a semiconductor nanocrystal solution processed at plastic-compatible temperatures.

CdSe is an ideal material for assessing the feasibility of printing semiconductor nanocrystal solutions as precursors to thin polycrystalline films for TFTs. Vacuum-deposited CdSe has been used as the active layer in TFTs since the 1960s. Flexible CdSe TFTs have been fabricated on aluminum foil, plastic, and even paper (*16*). Furthermore, CdSe semiconductor nanocrystals are very well characterized and their preparations are well developed (*17*).

Although several nanocrystal syntheses yield II-VI semiconductor quantum dots with tight size distributions, we have not found the pyrolytic methods (*18*, *19*) to be suitable for this application. The heavy coordinating solvent used in these reactions—trioctylphosphine oxide (TOPO)—cannot be entirely removed by cap exchange procedures (*19*, *20*). TOPO is not volatile and decomposes when heated, leading to carbon impurities in sintered polycrystalline films (*14*). Alternate synthetic methods do not offer the same degree of size control as the pyrolytic syntheses and generally have tightly bound organic surface groups as well.

The most appropriate synthesis for II-VI semiconductor nanocrystals that we are aware of is the CdTe metathesis reaction that has been demonstrated between CdI_2 and Na_2Te in methanol (*21*). The product from this synthesis has been spray-deposited as a part of solar cell fabrication (*22*). Unfortunately, the nanocrystal size distribution from this synthesis is broad, and most of the particles are too large to be expected to melt at plastic-compatible temperatures. We have developed a modified metathesis reaction that yields smaller particles with lower melting points. Modifications of micelle (*23*) and pyrolysis (*18*, *19*) preparations should also provide nanocrystals appropriate for low-temperature melting or sintering.

The metathetic route is modified by introducing a low-boiling coordinating solvent into the reaction medium. Pyridine was found to work well, retarding particle growth and tightening the size distribution (Fig. 1). Pyridine loosely caps the nanoparticle product and readily desorbs and volatilizes to leave an organic-free nanocrystal (*19*). A typical synthesis is carried out at room temperature in a nitrogen-filled glove box. Methanolic solutions of the reagents CdI_2 and Na_2Se are prepared (at 7.4 mM concentrations), and a reaction vessel is charged with pyridine. Equimolar amounts of the reagents are then added to the reaction vessel. Pyridine generally constitutes one-third of the total reaction volume. The reaction proceeds instantaneously, forming a yellow solution that quickly precipitates the nanocrystalline product. The nanocrystals are then isolated by centrifugation and decanting of the supernatant, and the soluble byproduct, NaI, is removed by repeatedly dispersing the product in methanol and isolating the particles after centrifugation and decanting. After dissolution of the nanocrystals in pyridine, they are precipitated by addition of hexane and again isolated by centrifugation and decanting. Finally, the nanocrystals are redissolved in pyridine and filtered through a 0.2-μm filter.

Absorption spectroscopy reveals that after the particles are isolated and dissolved in pyridine, they continue to ripen, favoring a few select size species (Fig. 1). These bottlenecks in the growth series result from the thermodynamic stability of a complete, closed structural shell (*18*). The optical features match those reported for the smallest particles observed in pyrolytic syntheses (*18*), which are believed to be extremely small tetrahedral clusters less than 2 nm across with structures similar to those reported for discrete CdS (*13*) and CdSe (*24*) species. These cluster species are inherently nonstoichometric, but energy-dispersive x-ray

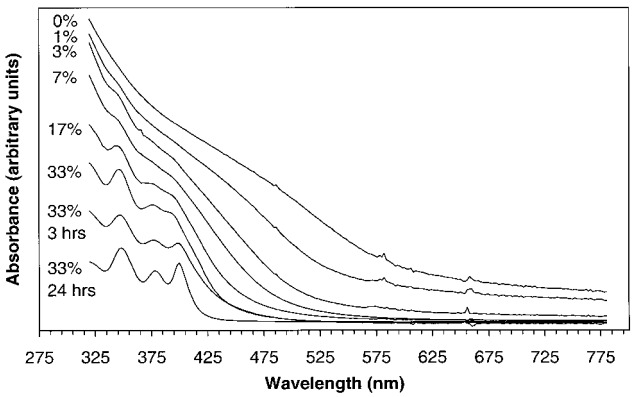

Fig. 1. Absorption spectra covering ultraviolet and visible wavelengths, demonstrating the influence of pyridine on the formation of CdSe nanocrystals by metathesis. The uppermost spectrum represents a sample synthesized without any pyridine, and pyridine concentration increases for each subsequent spectrum as follows: 1, 3, 7, 17% and a maximum of 33% by volume for the bottom three spectra. As the concentration of pyridine increases, the average particle size decreases and absorption features shift to lower wavelengths (*18*). Of the three spectra of particles synthesized in 33% pyridine, the uppermost spectrum was taken immediately after the reaction, the middle spectrum three hours after the reaction, and the lowest spectrum a day after the reaction. The sharpening of spectral features with increasing time indicates a reduction of the size distribution (*18*) as the particles ripen.

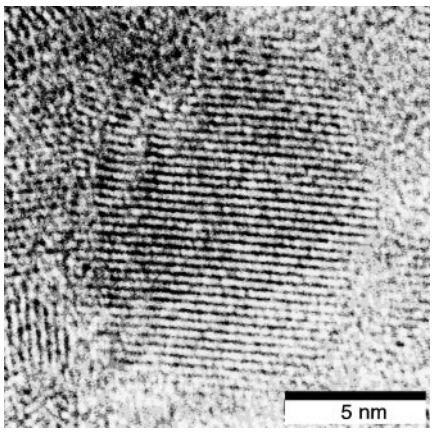

Fig. 2. The TEM image showing long-range crystal order resulting from a 30-min heat treatment at 350°C of CdSe nanocrystals formed by metathesis in pyridine.

spectroscopy (EDX) finds that the Cd:Se stoichiometry is 1:1. This indicates that a number of species exist to produce a balanced stoichiometry over the whole sample. EDX also indicates that there is no residual Na or I from the synthesis.

Previous work on the melting point depression of CdS nanocrystals found that they sinter together to form a polycrystalline bulk material with domains no larger than the original particles (*11*). The surface of the nanocrystal has a lower melting point than its core, and sintering occurs at about two-thirds of the suppressed melting temperature (*12*). Although the domains that initially form may be the same size as the nanocrystals, in this work we used a 30- to 60-min heat treatment that served as both a sintering and an annealing step. Transmission electron microscopy (TEM) showed that the heat treatment produces crystalline areas as large as 15 nm across (Fig. 2), which is comparable to grain sizes reported for vapor-deposited CdSe TFTs (*25*). The TEM image is markedly different from images of unheated nanocrystals. Unheated nanocrystals have extremely small crystalline areas near the detection limit of the microscope. We have not observed grain growth with ~20 Å CdSe nanocrystals synthesized by pyrolysis, which indicates that the residual TOPO from the pyrolytic synthesis hinders grain growth.

X-ray photoelectron spectroscopy (XPS) of films derived via the metathetic route confirms that the Cd:Se stoichiometry is near 1:1 and detects I in the sintered films. Although EDX does not detect I, XPS is a surface technique and it is possible that I diffuses to the surface during the anneal. Such behavior has been documented for Cr (*26*). Like Cr, I is expected to act as an n-type dopant.

After synthesis, device fabrication is completed in the glove box. A single drop of the pyridine CdSe nanocluster solution is deposited onto the area between the source and drain electrodes of a TFT test structure (Fig. 3). The semiconductor nanocrystals are heated by placing the wafer on a hot plate. Various heat treatments ranging from 150 to 350°C have been used to sinter the nanocrystals in the channel. Upon cooling, Norland Optical Adhesive 73, a photocurable polymer adhesive, is deposited and cured to encapsulate the active area of the TFT. Unencapsulated devices do not exhibit a field effect.

The TFTs are probed in air in a dark box at room temperature. Those heated to 150°C do not exhibit a field effect and are indistinguishable from control TFTs fabricated without any heating of the deposited nanocrystals. TFTs processed at 250°C do exhibit a field effect, with higher mobilities observed with higher temperature treatments.

A TFT ramped from room temperature at 80°C/min and held at 350°C for 1 hour shows an ON/OFF ratio of 3.1×10^4, a linear regime mobility of 1 $cm^2\ V^{-1}\ s^{-1}$, a threshold voltage of 6.7 V, and a subthreshold slope of ~7 to 10 V per decade (Fig. 4A). Several devices with similar characteristics have been fabricated. The hysteresis mechanism is currently under investigation; it may be due to interface states at the semiconductor/insulator interface or simply due to poor encapsulation and oxidation of the TFT. Vapor-deposited CdSe TFTs exhibit similar hysteresis (*27*, *28*). The negative resistance seen in the saturation region of the I_D-V_{DS} characteristics of the same device is also likely to be caused by hysteresis in the semiconductor film (Fig. 4B).

The mobility of these TFTs is approximately an order of magnitude larger than the mobility of printed organic TFTs. Although these results represent the highest printed mobilities to date, the peak mobilities observed in nanocrystal-derived CdSe films are more than two orders of magnitude lower than the mobilities of vapor-deposited CdSe films. Further improvements in nanocrystal solution purity and processing techniques are expected to yield further increases in field-effect mobility.

Although our processing temperatures are compatible with high–glass transition temperature plastic substrates such as polyimide, they are not compatible with transparent plastics. However, laser annealing of semiconductor nanocrystals could be used to further reduce processing temperatures and to improve film quality. The CdSe thin films described in this report were cast from solution with a micropipet, but we have also been able to pattern nanoparticle solutions through drop-on-demand ink-jet printing (80-μm drops, 10-μm spacing), direct optical patterning (2-μm features), and stamping (250-nm features) (*29*).

Finally, we note that we have successfully applied these techniques to fabricate TFTs using the semiconductor CdTe. Because the size-dependent melting point depression in these II-VI semiconductors is a general effect observed across a broad class of materials (*10*), the approach we have outlined is applicable to the printing of inorganic conductors and insulators as well as a wide variety of semiconductors, including Si, Ge, GaAs, and InP.

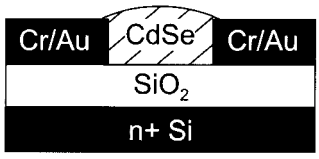

Fig. 3. Thin-film transistor schematic. The test structure is a coplanar inverted TFT composed of an n+ Si gate, 100-nm dry thermal SiO_2 oxide, and Cr/Au (10 nm/100 nm) source and drain contacts deposited by electron beam evaporation. The channel has a length (L) of 8 μm and a width (W) of 293 μm.

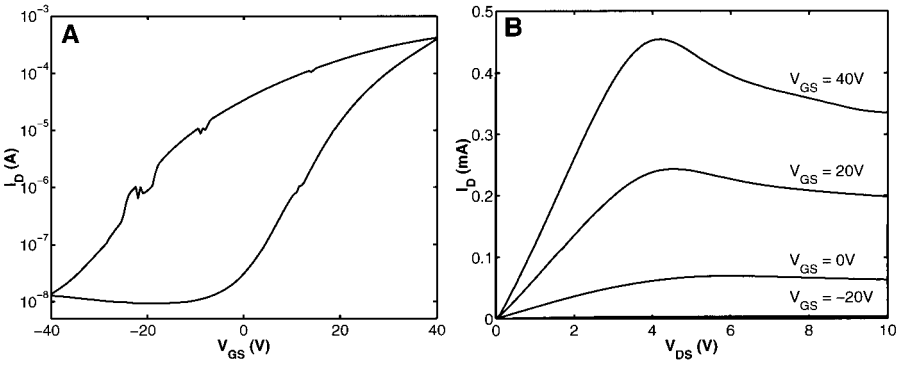

Fig. 4. Drain current versus gate source voltage (I_D-V_{GS}) and drain current versus drain source voltage (I_D-V_{DS}) characteristics of a TFT. (**A**) log I_D-V_{GS} indicates an ON/OFF ratio of 3.1×10^4 for a gate sweep of $V_{GS} = -40$ V to $V_{GS} = 40$ V at $V_{DS} = 2.5$ V. The subthreshold slope is ~7 to 10 V per decade and the hysteresis is clockwise. A linear regime mobility (μ) of 1 $cm^2\ V^{-1}\ s^{-1}$ is extracted by equating the slope of an I_D-V_{GS} plot to $(W/L)\mu C_{ox} V_{DS}$ at $V_{DS} = 2.5$ V, where C_{ox} is the capacitance of the gate oxide. A threshold voltage of 6.7 V is extracted from the V_{GS} intercept of an I_D-V_{GS} plot. (**B**) I_D-V_{DS} with a gate sweep from $V_{GS} = -40$ V to $V_{GS} = 40$ V in 20-V steps.

References and Notes

1. Z. Bao, A. Dodabalapur, A. J. Lovinger, *Appl. Phys. Lett.* **69**, 4108 (1996).
2. C. J. Drury, C. M. J. Musaers, C. M. Hart, M. Matters, D. M. de Leeuw, *ibid.* **73**, 1 (1998)
3. H. Sirringhaus, N. Tessler, R. H. Friend, *Science* **280**, 1741 (1998).
4. F. Garnier, R. Hajlaoui, M. El Kassmi, *Appl. Phys. Lett.* **73**, 1721 (1998).
5. Y.-Y. Lin, D. J. Gundlach, S. F. Nelson, T. N. Jackson, *IEEE Electron Device Lett.* **18**, 606 (1997).
6. A. Dodabalapur *et al.*, *Appl. Phys. Lett.* **73**, 2 (1998).
7. *Mat. Res. Soc. Symp. Proc.* **472**, 439 (1997).
8. A. P. Alivisatos, *MRS Bull.* **23**, 18 (February 1998).
9. Ph. Buffat, J.-P. Borel, *Phys. Rev. A* **13**, 2287 (1976).
10. *Mat. Res. Soc. Symp. Proc.* **206**, 271 (1991).
11. A. N. Goldstein, C. M. Echer, A. P. Alivisatos, *Science* **256**, 1425 (1992).
12. A. N. Goldstein, *Appl. Phys. A* **62**, 33 (1996).
13. N. Herron, J. C. Calabrese, W. E. Farneth, Y. Wang, *Science* **259**, 1426 (1993).
14. *Mat. Res. Soc. Symp. Proc.* **426**, 349 (1996).
15. T. Vossmeyer *et al.*, *J. Phys. Chem.* **98**, 7665 (1994).
16. T. P. Brody, *Proc. SPIE—Int. Soc. Opt. Eng.* **1664**, 2 (1992).
17. L. E. Brus, *J. Phys. Chem. Solids* **59**, 459 (1998).
18. C. B. Murray, D. J. Norris, M. G. Bawendi, *J. Am. Chem. Soc.* **115**, 8706 (1993).
19. J. E. Bowen Katari, V. L. Colvin, A. P. Alivisatos, *J. Phys. Chem.* **98**, 4109 (1994).

20. M. Kuno, J. K. Lee, B. O. Dabbousi, F. V. Mikulec, M. G. Bawendi, *J. Chem. Phys.* **106**, 9869 (1997).
21. *Mat. Res. Soc. Symp. Proc.* **272**, 229 (1992).
22. D. L. Schultz *et al.*, *Am. Inst. Phys. Conf. Proc.* **394**, 683 (1997).
23. M. L. Steigerwald *et al.*, *J. Am. Chem. Soc.* **110**, 3046 (1998).
24. S. Behrens *et al.*, *Angew. Chem. Int. Ed. Engl.* **35**, 2215 (1996).
25. A. Van Calster, A. Vervaet, I. De Rycke, J. De Baets, *J. Cryst. Growth* **86**, 924, (1998).
26. G. J. Scilla, J. J. Wysocki, *J. Vac. Sci. Technol.* **18**, 37 (1981).
27. C. Reita, *Inf. Display* **2**, 10 (1993).
28. T. P. Brody, *ibid.*, p. 5.
29. J. M. Jacobson *et al.*, invited talk given at the annual meeting of the Materials Research Society, Session G, on 29 November 1999 in Boston, MA.
30. We thank M. Bawendi, D. Antoniadis, C. Leatherdale, J. Taylor, S. Griffith, B. Hubert, and the staff at the Microsystems Technology Laboratory (MTL) for helpful discussion; M. Frongillo for assistance with TEM; L. Shaw for assistance with XPS; and M. Strojwas for help in device probing. TFT test structures were fabricated at the MTL at MIT. This work made use of MRSEC Shared Facilities supported by NSF under award number DMR-9400334. Supported by Defense Advanced Research Project Agency contract DABT63-99-C-0033 and by the MIT Media Lab's Things That Think (TTT) consortium. B.A.R. is partially supported by a graduate research fellowship from Motorola; B.N. is partially supported by a graduate research fellowship from NSF.

18 June 1999; accepted 14 September 1999

Bidirectional Semiconductor Laser

Claire Gmachl,* Alessandro Tredicucci, Deborah L. Sivco, Albert L. Hutchinson, Federico Capasso, Alfred Y. Cho

A semiconductor laser capable of operating under both positive and negative bias voltage is reported. Its active region behaves functionally as two different laser materials, emitting different wavelengths, depending on the design, when biased with opposite polarities. This concept was used for the generation of two wavelengths (6.3 and 6.5 micrometers) in the midinfrared region of the spectrum from a single quantum cascade laser structure. The two wavelengths are excited independently of each other and separated in time. This may have considerable impact on various semiconductor laser applications including trace gas analysis in remote sensing applications with differential absorption spectroscopy.

Most optoelectronic semiconductor devices, such as conventional semiconductor lasers, light-emitting diodes, and solar cells, are bipolar; that is, they contain a combination of semiconductor layers doped with donor impurities (n-type doped) and with acceptor impurities (p-type doped). The resulting built-in electrostatic potential provides an inherent directionality to these devices and renders them functional for a specific voltage polarity. On the contrary, unipolar optoelectronic devices offer the possibility of bidirectional use. The invention and development of unipolar lasers known as quantum cascade (QC) lasers (*1, 2*) have attracted considerable attention because they can be designed to operate in an extremely broad spectral range (the entire midinfrared spectrum). This is done by controlling the layer thicknesses rather than the material composition, with band-structure engineering (*3*) and molecular beam epitaxy (*4*). In addition, the generation of many laser photons per injected electron above threshold, due to the cascading of active regions, is responsible for the unprecedented power of QC lasers (*2, 5*).

Here, a bidirectional, unipolar semiconductor laser is presented. Unlike all other semiconductor lasers, including QC lasers fabricated to date (*2*), it operates as a light source under both positive and negative bias voltage. In addition, the operating wavelength can be made different in the two polarities. These features provide functionality not available in conventional semiconductor lasers, opening the door to many useful applications (*6*).

In QC lasers, the optical transition takes place between quantized states in the conduction band of a multiple quantum well structure (*1, 2*). The emission wavelength is determined by the energy level difference, which is controlled by the well and barrier thickness and the applied electric field. In general, reversing the applied bias in standard QC lasers alters the energy level structure, thus preventing laser action. The device presented in this paper operates instead as a different QC laser in each polarity.

In the diagram describing the basic principle of operation of the bidirectional QC laser (Fig. 1), a portion of the conduction band structure, two active regions with the connecting injector region, is shown. QC lasers typically contain a stack of $N \sim 30$ periods of alternating active regions and injectors (*2, 5*). In the present design, under an appropriate applied positive bias (Fig. 1A), laser action takes place from level G_+ to level 1, through a photon-assisted tunneling or diagonal transition (wavy arrow) because the two states have reduced spatial overlap (*7*). Level 1 is the ground state of the active region quantum well, whereas G_+ is the ground state of the miniband—a dense manifold of electronic levels in the superlattice injector. This miniband is designed so that under application of a suitable electric field, G_+ is spatially localized close to the injection barrier (*7*). The emitted photon energy is controlled, for a given active region quantum well, by the thickness of the injector layers in the immediate vicinity of the injection barrier and by the applied electric field. A reversal of the bias polarity (Fig. 1B) will localize the injector ground state G_- at the opposite end of the injector miniband. With an injector entirely symmetric around its center, G_+ and G_- would be equivalent, and the laser wavelength would be the same in both polarities. If, however, the injector regions are designed as asymmetric, the energy position of G_- will be different than that of G_+, leading to different laser wavelengths $\lambda_\pm$.

The exact layer design, a portion of the band structure, and the moduli squared of the relevant wave functions of sample D2520 are shown in Fig. 2. We briefly discuss the design parameters that are important for bidirectional, dual-wavelength operation. An in-depth description of QC lasers based on photon-assisted tunneling, including the implications of the reduced spatial overlap of the electron wave functions involved in laser action, can be found in (*7*). The important quantity in the calculation of the threshold gain of QC lasers is $k_\pm = z_\pm^2 E_\pm \tau_\pm$. The product of the first two factors, that is, the square of the optical matrix element $z_\pm$ and the energy of the transition $E_\pm$, is proportional to the oscillator strength $f_\pm$. $\tau_\pm$ is the lifetime of level $G_\pm$, determined mainly by the relaxation time from $G_\pm$ to level 1, due to the emission of a longitudinal optical phonon. The indices imply that these values can be set independently for each bias direction. If one is interested in a device with two different emission wavelengths, that is, $E_+ \neq E_-$, but comparable threshold current and voltage (*8*), then $z_\pm$ and $\tau_\pm$ need adjustment to achieve $k_- = k_+$ at the same applied electric field, regardless of the polarity.

For sample D2520, shown in Fig. 2 under an electric field of ± 90 kV cm^{-1} corresponding to the threshold, we calculated $z_+ = 0.35$ nm, $z_- = 0.32$ nm, $\tau_+ = 46$ ps, $\tau_- = 64$ ps, and $E_+ = 198$ meV, $E_- = 173$ meV, respectively. This results in $k_+ = 1.12$ nm^2 ps eV and $k_- = 1.14$ nm^2 ps eV, which are sufficiently close to each other to suggest very similar threshold currents. Population

Bell Laboratories, Lucent Technologies, 600 Mountain Avenue, Murray Hill, NJ 07974, USA.

*To whom correspondence should be addressed. E-mail: cg@lucent.com